Development of Advanced Simulation Methods for Solid Earth Simulations

Project Representative
Akira Kageyama The Earth Simulator Center, Japan Agency for Marine-Earth Science and Technology

Authors
Akira Kageyama *1, Mamoru Hyodo *1, Mikito Furuichi *1, Takehiro Miyagoshi *1, Nobuaki Ohno *1, Masanori Kameyama *2 and Yosuke Ito *3

*1 The Earth Simulator Center, Japan Agency for Marine-Earth Science and Technology
*2 Ehime University
*3 University of Tokyo

We are developing advanced numerical algorithms and codes for solid earth simulations. One of the most important findings in this fiscal year is a new type of dynamo in the low Ekman number regime of geodynamo simulation. Our spherical grid, Yin-Yang grid, used in this geodynamo simulation is also applied to the spherical mantle convection simulation. The basic algorithm for this spherical mantle convection is also our own, ACuTE algorithm. We have also developed a basic algorithm to solve the time development of visco-elastic fluid motion. The validation test was performed by applying it to a fluid rope coiling problem. We have also developed a new code for the earthquake cycle simulation by the finte element method. By combining analytical solution and GeoFEM-based numerical solution, we could accurately evaluate fault stress under heterogenous structure.

Keywords: geodynamo, mantle convection, ACuTE method, Yin-Yang grid, visco-elastic fluid

1. High Resolution Geodynamo Simulation by Yin-Yang Grid with low Ekman number

The Yin-Yang grid [1, 2] is a kind of overset grid system on the spherical geometry. We have applied it to geodynamo simulations [3, 4, 5] and mantle convection simulations [6, 7].

In this fiscal year, we performed large scale geodynamo simulations using the Yin-Yang geodynamo code. Figure 1 shows a snapshot of high resolution simulation on 512 nodes of the Earth Simulator. The details of the code, especially on the optimization for the vector/parallel processing can be found in [3]. The grid size of the simulation is $N_r \times N_\theta \times N_\phi \times 2 = 511 \times 514 \times 1538 \times 2$, where N_r, N_θ, N_ϕ are grid size in radial, latitudinal, and longitudinal directions. The last factor × 2 is for Yin and Yang. Due to this high resolution, very low Ekman number (which is the ratio of diffusion speed/rotation speed) calculation can be performed. The Ekman number in this simulation is $E = 4.7 \times 10^{-7}$, which is the lowest value in past geodynamo simulation studies. From this simulation we found new convection, current and magnetic field structure.

What are shown in Fig. 1(a) are current field (blue lines), cross sections of vorticity distribution on the equatorial plane (color contour) with the sphere near the inner core. The red and blue area on the equatorial plane is for positive and negative vorticity, respectively, or more strictly, the vorticity component parallel to the rotation axis. The convection pattern drastically changes from past laminar geodynamo simulations which showed formation of positive and negative vorticity columns side by side. The feature of the vorticity distribution in Fig. 1 is multiple sheet-like structure elongated in the perpendicular direction to the rotation axis, since the velocity field (and therefore the vorticity field, too) is nearly two-dimensional due to the strong constraint of the rotation. The strong magnetic field is generated by these "plume sheets".

Magnetic field is fully amplified by the magnetohydrodynamic (MHD) dynamo action by the time when the snapshot of Fig. 1 is taken. The total magnetic energy integrated over the spherical shell region, or the outer core, is almost nearly equal to the convection flow energy.

The current fields and magnetic fields generated under the convection motion also have very characteristic structures. Almost all current fields seen in Fig. 1(a) and (b) form helical coil structure through which a bundle of magnetic flux tubes are formed. Fig. 1(c) shows one of helical current coils (red tubes) and magnetic field lines (blue tubes). Nearly

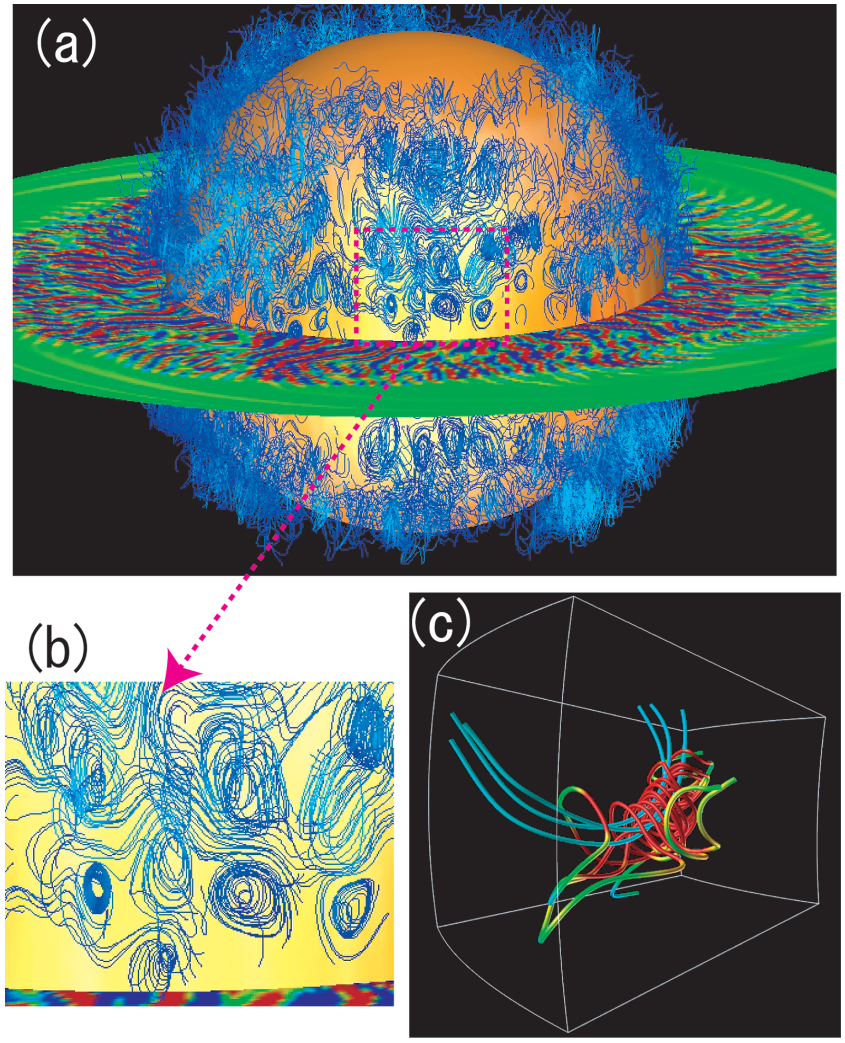

Fig. 1 A high resolution geodynamo simulation using Yin-Yang grid. Ekman number $E = 4.7 \times 10^{-7}$. (a) The color distribution of blue–green–red shows the vorticity component parallel to the rotation axis on the cross section of the equatorial plane. The current field lines are also shown as blue lines with the sphere near the inner boundary. (b) The magnified image of a part of (a). (c) One of the helical current coils (red tubes) and magnetic field lines (blue tubes).

straight magnetic flux exists inside the helical current coil. This means a magnetic flux tube is formed and helical current flows the edge of the flux tube.

In order to analyze the relation between helical current coils and the generation of the magnetic field by the sheet plume convection, we examined the distribution of $D \equiv -\mathbf{v} \cdot (\mathbf{j} \times \mathbf{B})$ in the spherical shell, where $\mathbf{v}$, $\mathbf{j}$, $\mathbf{B}$ are the flow velocity, electric current density, and magnetic field, respectively. The quantity D is the work rate done by the flow against the $\mathbf{j} \times \mathbf{B}$ force. In other words, D is positive where the flow energy is converted into the magnetic energy. The D distribution of the data at the same snapshot as Fig. 1 is shown in Fig. 2, as green surfaces. By analyzing D distribution we found that the positions of positive D well match the positions of helical current coils. They also appear in the middle latitude both in the northern and southern hemispheres. Their distribution is approximately symmetric about the equatorial plane. We found that the plume sheet

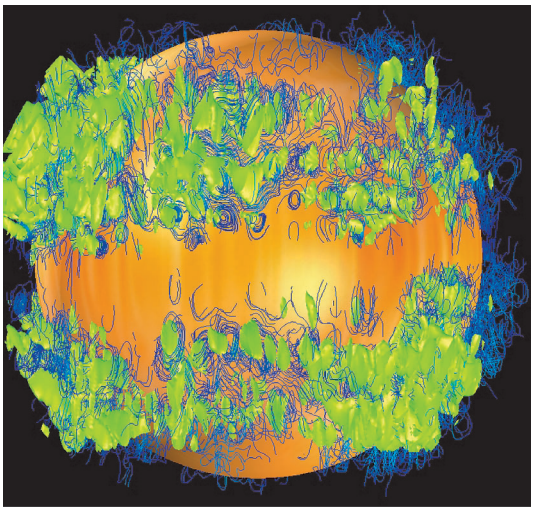

Fig. 2 The blue lines show current fields, which is the same data as Fig. 1. The green regions stand for regions where magnetic field is generated by the energy conversion from convection kinetic energy into the magnetic energy. The positions of positive D well match the positions of helical current coils.

convection motion bundles and stretches the magnetic fields. Then magnetic flux is amplified and magnetic flux tubes are formed.

The new findings in this fiscal year including convection structure (sheet plumes), the current field structure (helical coils), and the magnetic field structure (localized straight flux tubes) are summarized in our recent paper [8].

2. New Simulation Code of Mantle Convection in Spherical Shell Geometry by Combination with ACuTE and Yin-Yang Grid Technologies

In fiscal year 2006, we had started a development of a new simulation code of mantle convection in a spherical shell geometry which is suitable for large-scale and parallel numerical calculations. The new code came out from an integration of the ACuTE method [9, 10, 11, 12, 13, 14] into the Yin-Yang grid [1, 2]. Through the activities in fiscal year 2006, we had successfully carried out several preliminary calculations by using a prototype version of the code with moderate mesh divisions.

In this fiscal year, we have further optimized and tested the new simulation code in order to demonstrate its applicability toward large-scale numerical simulations of mantle convection under realistic conditions. The code optimization is largely aimed at enhancing the vectorization of the ACuTE smoothing iterations employed in the multigrid method for the solution of flow fields. During the multigrid cycles, the smoothing calculations on coarse grid levels play an important role in reducing (or smoothing out) the long-wavelength errors sufficiently fast with low computational costs. From the viewpoint of vectorization, on the other hand, the computations on coarse grid levels are less efficient owing to small loop lengths coming from small problem sizes. In order to improve the vectorization performance, we enlarged the loop lengths of the ACuTE smoothing iterations by collapsing 3-fold (r, θ, ϕ) or 4-fold (r, θ, ϕ and Yin-Yang) loops in spatial dimensions into unnested ones. By this optimization, we had successfully carried out convection simulations with the spatial resolutions higher than ever studied by the numerical codes using the finite-difference and/or finite-volume discretizations. As summarized in Fig. 3, the optimization processes also enabled us to confirm the accuracy of the present numerical code with the spatial mesh divisions of up to 128 × (128 × 384 × 2) in radial and horizontal directions, respectively.

In addition, we calculated a time-dependent convection for a stronger temperature-dependent viscosity, as a first attempt to the numerical simulation under more realistic conditions. Figure 4 shows the snapshots of lateral thermal anomalies at for time instances from the quasi-static stages where a thermal equilibrium is almost achieved. As has been shown in the figure, we had successfully reproduced the change in con-

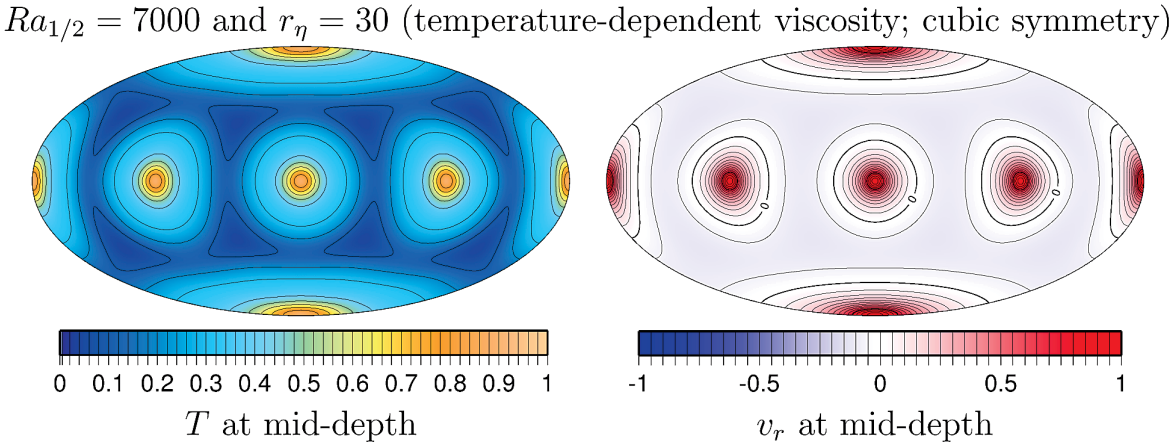

Model	$r \times (\theta \times \phi)$	Nu	$V_{\rm rms}$	$T_{\rm av}$	$T_{\rm i,max}$	$T_{\rm i,min}$	$v_{\rm i,max}$	$v_{\rm i,min}$
St06	Extrapolated	3.2976	24.2435	0.25704	0.88740	0.04223	137.773	-16.234
KKS	$32\times(2\times32\times96)$	3.2915	24.1675	0.26221	0.85126	0.04463	127.386	-16.750
KKS	$64\times(2\times64\times192)$	3.2959	24.2300	0.25844	0.87495	0.04293	134.180	-16.369
KKS	$128\times(2\times128\times384)$	3.2969	24.2435	0.25728	0.88439	0.04231	136.982	-16.255

Fig. 3 Summary of numerical results of steady-state convection with cubic symmetry for $Ra_{1/2}$ = 7000 and weakly temperature-dependent viscosity of r_η = 30 in a spherical shell whose ratio of inner and outer radii is r_i/r_o = 0.55. Shown are the Hammer plots of the distribution of temperature T (top left) and the fluid velocity in radial direction v_r (top right) at the mid-depth of the spherical shell (r/r_o = 0.775), and the table comparing the global (Nusselt numbers Nu, root-mean-squared velocities $V_{\rm rms}$ and average temperature T_{av}) and local (maximum/minimum values of the interior temperature $T_{i,\,\rm max/min}$ and of the radial velocity $v_{i,\,\rm max/min}$) quantities (bottom). In the table, the symbol "KKS" indicates the results by the present code, while "St06" indicates the results summarized by Stemmer and others in 2006. Note also that plotted in the top-right are the values of vr scaled by its maximum absolute value max(|vr|) at the depth.

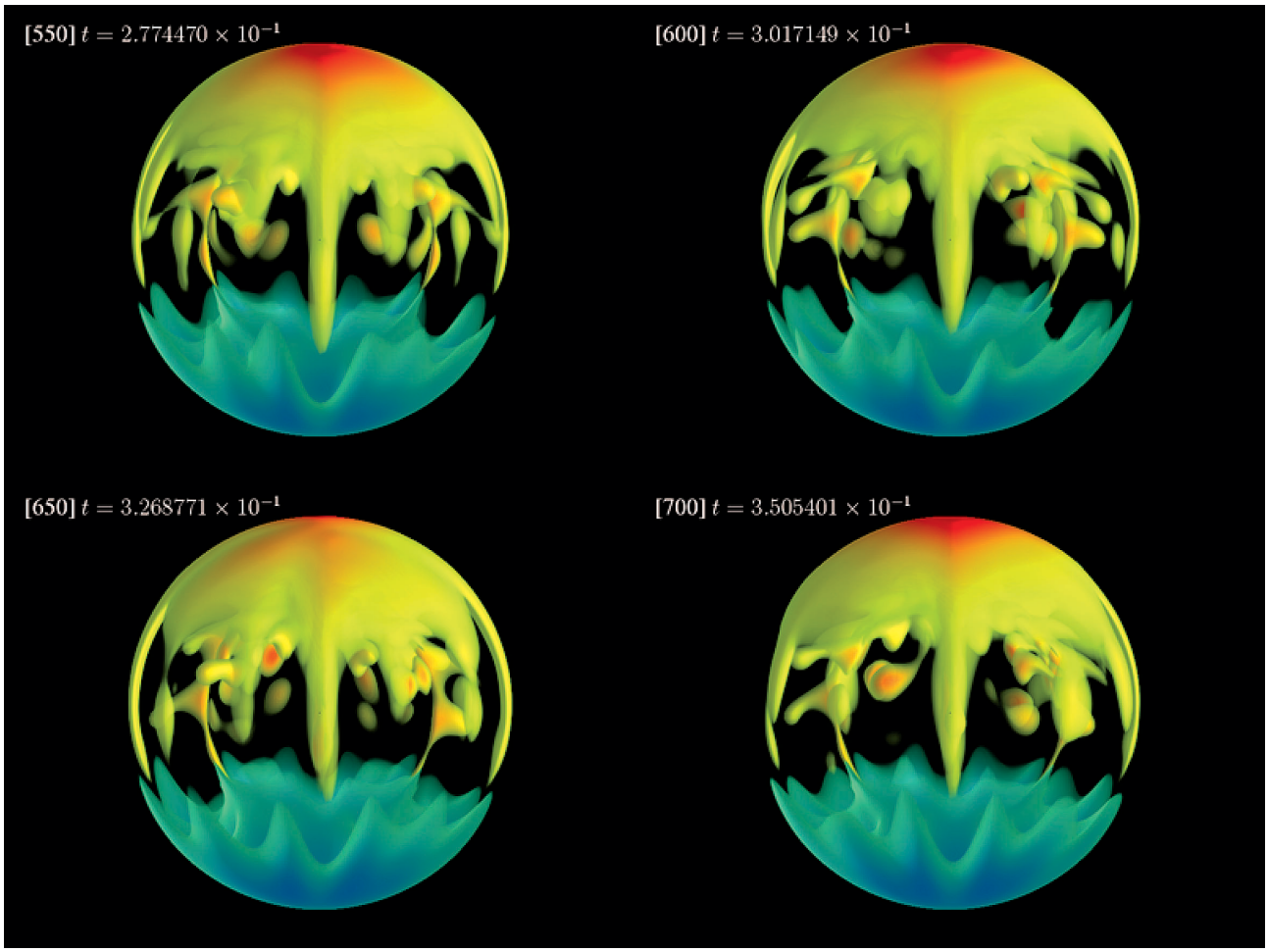

Fig. 4 Snapshots of flow patterns of time-dependent convection for strongly temperature-dependent viscosity with $Ra_{1/2}$ = 500,000 and r_η = 100,000. Shown are the three-dimensional plots of the distributions of lateral thermal anomalies $\delta T \equiv T - \langle T \rangle$, where $\langle T \rangle$ is the horizontally-averaged temperature at given r, at the elapsed times shown in the figure. Indicated in green to blue are the cold thermal anomalies with $\delta T < -0.1$, while in yellow to red are the hot anomalies with $\delta T > 0.1$.

vective flow patterns into the "Sluggish-Lid" regime with increasing the viscosity variations r_η up to 10,000, where the large-scale flow patterns become dominant.

3. Validity test of a Stokes flow solver by fluid rope coiling: toward plate-mantle simulation

Reproducing a realistic plate tectonics with mantle convection simulation is one of the great challenges in computational geophysics. We have been developed a three dimensional Eulerian numerical procedure toward plate-mantle simulation, which solve a finite deformation of the plate in the mantle convection. Our method, combined with CIP-CSLR-CS [15] and ACuTE Method [9, 10], enables us to solve advection and force balance equations even with large and sharp viscosity jump and visco-elastic properties, which plate and upper mantle boundary have.

One of the typical phenomena represented by our method is a fluid rope coiling event. The fluid rope coiling is the phenomenon that a thin downward stream of viscous fluid (fluid rope) is winded by an impact from the bottom, and continuously coils around the vertical axis. We propose to use the fluid rope coiling for the validation test of the simulation scheme. This event can be reproduced by a quite simple simulation setting: a highly viscous fluid is poured from a top sinking to the bottom plane through tenuous, relatively low viscous fluid. In the frame work of the Eulerian scheme, the fluid rope and surrounding air are treated as viscous (η_{rope}) and very low viscous (η_{air}) profiles respectively. Our method solve the complex force balances of the fluid rope and air, by a multigrid iteration technique of ACuTE algorithm. In addition, the CIP-CSLR advection scheme allows us to obtain a deforming shape of the fluid rope as a low diffusive solution, even in the Eulerian frame of reference.

Our validity test with this event can be used to estimate the accuracy of simulation method for the large and complex deformation in three dimensions. There is no standard of such a validation test for large non-linear deformation problems, because a simple analytical treatment like that of a Rayleigh-Taylor instability analysis is unavailable. We therefore compare our three dimensional simulation result

(3-D model) with the numerical solution of the equilibrium problem, in which a coiling motion of slender fluid rope is characterized by a set of ordinary differential equations of one independent spatial variable (1-D model).

We first show a qualitatively comparison of the 3-D model with 1-D model in Fig. 5. The shapes of the simulated fluid rope by the 3-D model are shown by the yellow transparent isosurface. On the other hand, the fluid rope by the 1-D model are expressed by the sequence of colored balls, where the color and size indicates the radius of the circular cross section. The agreement of two solution is confirmed by the overlap of the isosurface and colored balls.

For a purpose of quantitative comparison, we focus on the time development of the three fluid rope parameters: length of the rope l, angular velocity Ω and the curvature at end of the fluid rope κ_1. We have summarized a root mean squared (RMS) deviation between the results of the 3-D model and 1-D model in Table 1 for the several simulation settings. Compared with the result of 'case A', the cases with larger viscosity contrast of the 'case B' and finer resolution of 'case C', do not improve the deviation of rope properties so much. These results mean that the contributions of a viscous air and mesh size, are not the main reason for the disagreements of fluid rope properties. We thus conclude that our 3-D model of the 'case A' quantitatively captures the fluid rope coiling phenomenon.

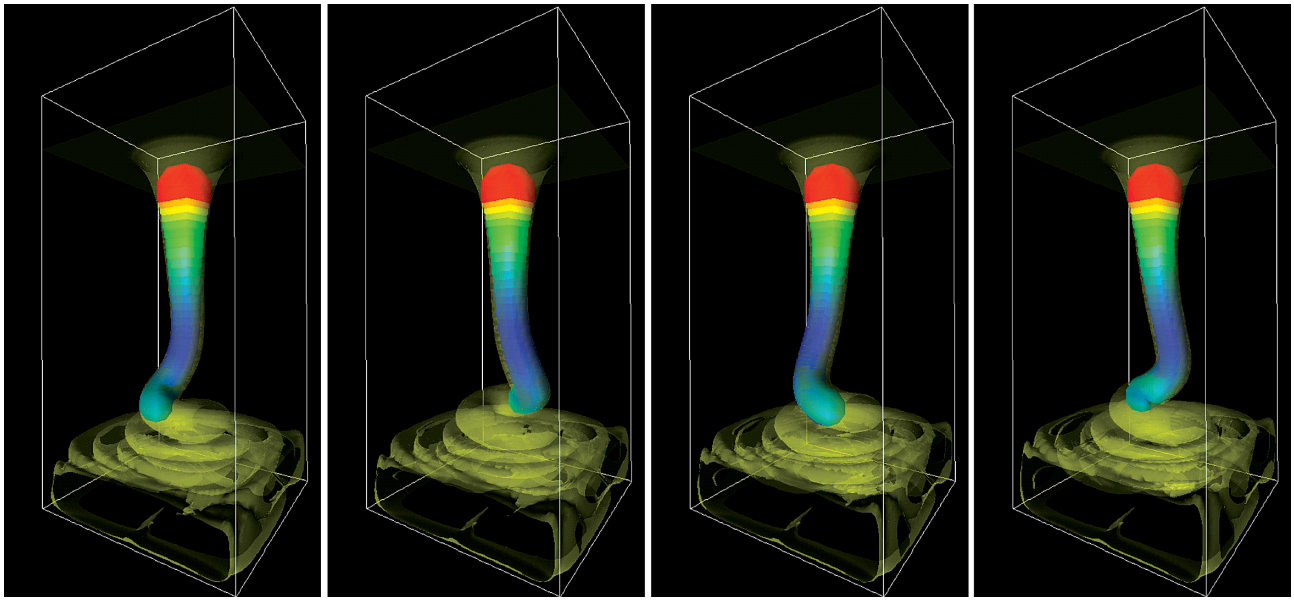

Fig. 5 Results of qualitative comparison for fluid rope properties. Semi-transparent yellow isosurface shows density distribution of rope fluid of 3-D model, and sequence of the colored balls (colored tube) shows solution of 1-D model. Size and color of ball express radius of fluid rope. Agreement of results between our 3-D model and 1-D model are represented by overlaps of isosurface and colored balls.

Table 1 Result of the comparison test.

Case	3-D model setting	RMS deviation
case A	box size $0.5 \times 0.5 \times 1.0$ mesh size $64 \times 64 \times 128$ $\eta_{rope}/\eta_{air} = 10^3$	$\Delta l = 0.49\%$ $\Delta\kappa_1 = 3.5\%$ $\Delta\Omega = 6.5\%$
case B	box size $0.5 \times 0.5 \times 1.0$ mesh size $64 \times 64 \times 128$ $\eta_{rope}/\eta_{air} = 10^4$	$\Delta l = 0.97\%$ $\Delta\kappa_1 = 8.2\%$ $\Delta\Omega = 8.4\%$
case C	box size $0.5 \times 0.5 \times 1.0$ mesh size $128 \times 128 \times 256$ $\eta_{rope}/\eta_{air} = 10^3$	$\Delta l = 0.64\%$ $\Delta\kappa_1 = 10.0\%$ $\Delta\Omega = 8.5\%$
case D	box size $0.5 \times 0.5 \times 1.0$ mesh size $32 \times 32 \times 64$ $\eta_{rope}/\eta_{air} = 10^3$	$\Delta l = 0.46\%$ $\Delta\kappa_1 = 6.3\%$ $\Delta\Omega = 22.4\%$

These results of validation test will be helpful to analyze our simulation results for the deformations of the plate in the mantle convection, such as a stagnation or folding at certain boundary layers.

4. Progress in Earthquake Cycle simulation

Numerical simulations aiming for reproducing the repetition of the stick-slip at a plate boundary are called as "earthquake cycle simulation". In such simulations, spatiotemporal development of the fault motion is determined by the difference of the fault shear stress caused by the surrounding material and the frictional resistance acting there. In many previous studies of earthquake cycles, the fault shear stress is commonly evaluated as the elastic interaction in a homogeneous elastic half-space. For several simple sub-surface structures like a homogeneous elastic half-space, stress field due to the unit dislocation on the particular position of the material is analytically obtained. Thus, the static stress field caused by the arbitrary distribution of dislocation on the fault is easily calculated as the surface integration of slip responses multiplied by the dislocation over the fault plane. Recently, the important effect of the inclusion of the known elastic heterogeneity on the surface deformation is reported by [16]. Hence, it is also indispensable to numerically incorporate the effect of the known elastic/viscoelastic heterogeneity, in order to execute a more realistic simulation especially for the Japanese islands located at the subducting plate boundary.

For this purpose, we began to develop a new "quasi-static" earthquake cycle simulation code utilizing GeoFEM system [17], and completed the prototype of simulation code in this fiscal year. The quasi-static simulation earthquake cycle simulation means that we always assume the equality of the fault frictional resistance and the quasi-static shear stress including the damping term for approximating the seismic wave radiation. This assumption yields the evolution equation for the fault slip. In our original simulation code, quasi-static equilibrium state is directly evaluated by solving the equilibrium equation in each time-step, and calculated stresses on finite element (FE) grids corresponding to the fault surface are used for the evolution of the fault slip or other variables on the fault plane obeying a rate-and state-dependent friction law. Updated fault slips are used as the boundary condition of the fault in the next time-step. An example of simulation results is shown in Fig. 6.

The advantage of our code is that we do not have to prepare slip response functions under a elastic/viscoelastic heterogeneous structure before the execution of numerical simulations. While, its disadvantage is a requirement of fine FE discretization, especially nearby the fault, for the accurate evaluation of stress field on the fault. Hence, as shown in Fig. 7, we applied an incorporation procedure of the analytic expression of stress field due to the slip in a simple structure and numeical solutions of stress field from two finite element analyses with different material properties.

To be concrete, the fault stress in a heterogeneous structure with a homogeneous fault zone is regarded as the sum of 1) changes in stress due to the fault slip in the homogeneous elastic model corresponding to the average elasticity of the fault zone, and 2) the additional stress term due to the effect of the heterogeneity surrounding the homogeneous fault zone. The former term can be evaluated accurately by using the analytic expression of slip responses in a homogeneous elastic half-space (Fig. 7a). While, the latter term is evaluated as the difference of FE solutions of a discrete heterogeneous model (Fig. 7c) and that of a discrete homogeneous model (Fig. 7b). If we apply the same FE grids for the homogeneous and heterogeneous FE analyses, we may be able to exclude numerical errors due to the FE discretization

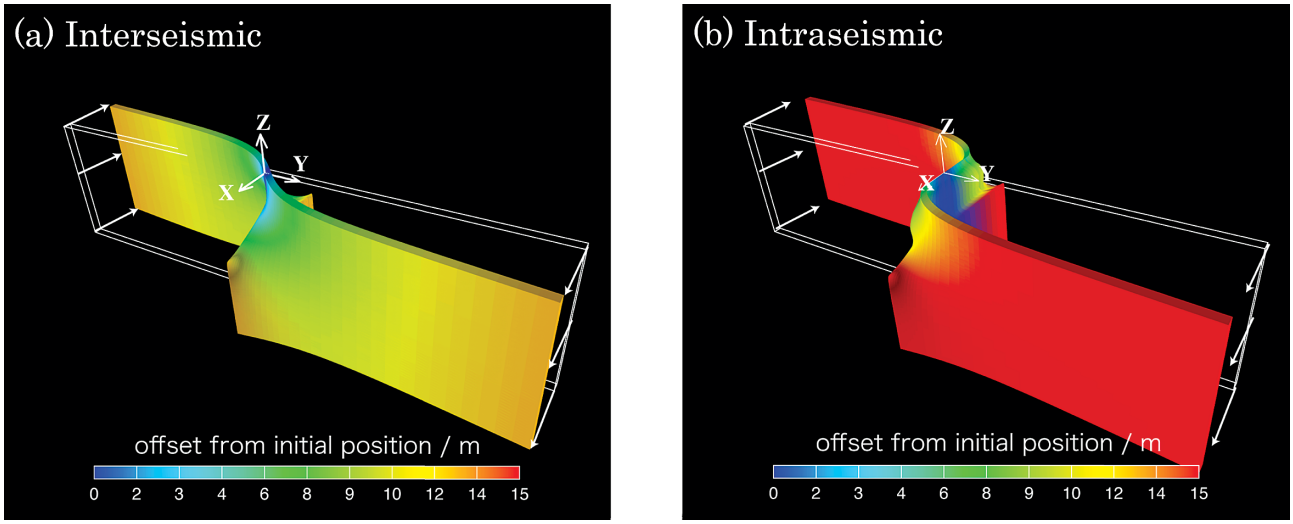

Fig. 6 An example of 3-D simulation implemented by our earthquake cycle simulation code. In this case, the fault is modeled as an infinitely long strike slip fault in the direction of X axis.

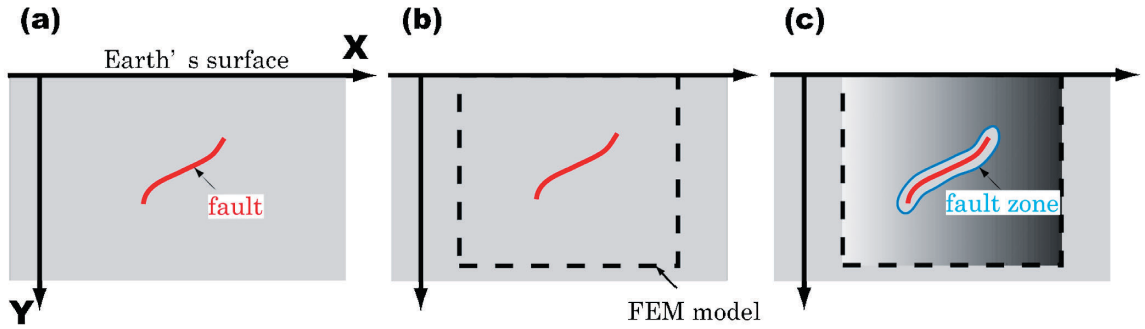

Fig. 7 A schematic illustrations for extracting the effect of a heterogeneous structure on the fault shear stress. The red line shown in each figure represents the fault plane obeying the rate-and state-dependent friction law. Dotted lines in Figs. (b) and (c) represent areas which are modeled by FE analysis. The same discretization of FE grids is assumed for model (b) and (c). (a) A homogeneous elastic half-space model. (b) A finite element model as a discretized model of (a). (c) A finite element model including the heterogeneous structure. The region surrounded by the blue line corresponds to the fault zone with a homogeneous elastic property similar to models (a) and (b).

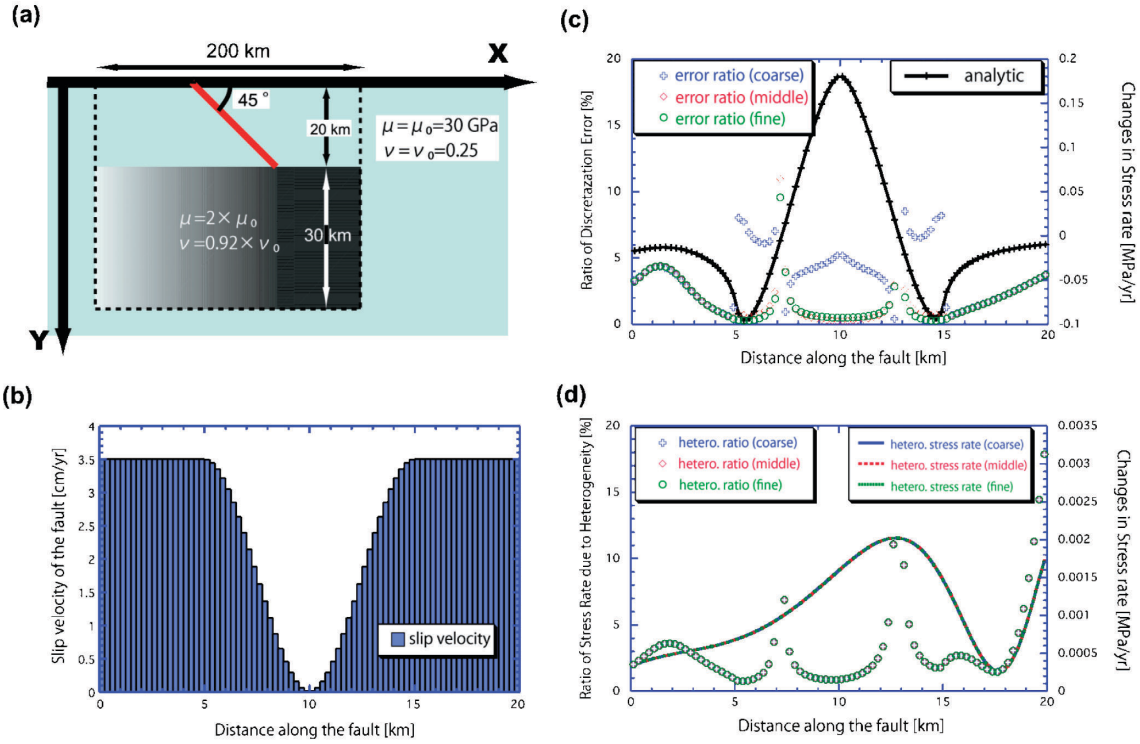

Fig. 8 A validation of the extraction procedure of the effect of a heterogeneous structure on changes in stress rate in 2-D plane strain case. (a) An example of a heterogeneous structure. The red line in the reference gray material represents the dipping fault, and the deeper material is assumed to have different elastic constants to shallow reference ones as an elastic heterogeneity. (b) Assumed distribution of the fault slip velocity with the boxcar-type basis function expansion. The total number of basis functions is 80 in the depth direction along the fault. (c) FE mesh dependence of discretization errors. The black line with crosses denotes the fault shear stress rate calculated by the analytic expression of the shear stress due to unit slip in a homogeneous elastic half-space and the distribution of the slip velocity shown in (b). Blue, red and green symbols are ratios of discretization errors to the analytic stress rate with different resolutions of FE meshes on the fault. (d) FE mesh dependence of stress rates caused by the heterogeneity. Blue, red and green symbols are ratios of shear stress rate caused by the heterogeneity to the analytic stress rate with different resolutions of FE meshes on the fault. While, three lines denote the differences of the heterogeneous and homogeneous FE solutions with different resolutions of FE meshes on the fault.

and extract only the effect of the heterogeneity surrounding the homogeneous fault zone by taking the difference of two FE solutions. In other words, the above examination means that we evaluate the discretization error from the difference of the homogeneous FE solution and analytic one, and exclude it from the heterogeneous FE solution solved with the same FE grid.

As a validation of the above method, we applied it to a program unit for specifying the fault slip in our earthquake cycle simulation code and evaluated the fault stress with different resolutions of FE meshes on the fault (an example case is denoted in Fig. 8). In this case, we tested three meshes

with different resolutions nearby the fault. Terms, "coarse", "middle" and "fine" in Fig. 8 represent the FE meshes with 2, 4, 8 elements among a boxcar-type basis function on the fault, respectively. Though the dependence of resolutions of FE meshes appears in discretization errors in Fig. 8c, even in the most coarse FE mesh case, almost the same value of stress rate is obtained compare to more finer mesh cases (see Fig. 8d), which means our procedure works good.

5. Other topics and publications

Modeling flows in the Earth's interiors requires its rheological properties. Lower mantle has over 50% volume of the whole Earth, though it's rheological properties are poorly known. Approach of the project for the project is getting diffusive properties lower mantle minerals by reproducing their self-diffusions by molecular dynamics (MD) simulations. This approach has been attempted for MgO periclase firstly in past fiscal years[18]. Simulation works in this fiscal year mainly targets $MgSiO_3$ perovskite. Through the simulation works, we have got new insight of lower mantle rheology[19]. It is expected that the new insight helps clarifying Earth's dynamics furthermore, especially with help of computational fluid dynamics.

We have also performed study on scientific visualization for solid earth simulation data [20, 21].

References

[1] Akira Kageyama and Tetsuya Sato. "Yin-Yang grid": An overset grid in spherical geometry. *Geochem. Geophys. Geosyst.*, 5(9):1–15, 2004.

[2] Akira Kageyama. Dissection of a sphere and Yin-Yang grids. *J. Earth Simulator*, 3:20–28, 2005.

[3] Akira Kageyama, Masanori Kameyama, Satoru Fujihara, Masaki Yoshida, Mamoru Hyodo, and Yoshinori Tsuda. A 15.2 TFLOPS simulation of geodynamo on the earth simulator. pages 35–43, Nov.2004.

[4] Akira Kageyama and Masaki Yoshida. Geodynamo and mantle convection simulations on the earth simulator using the Yin-Yang grid. *J. Physics: Conference Series*, 16:325–338, 2005.

[5] Akira Kageyama. Yin-Yang grid and geodynamo simulation. pages 688–692. 2005.

[6] Masaki Yoshida and Akira Kageyama. Application of the Yin-Yang grid to a thermal convection of a boussinesq fluid with infinite Prandtl number in a three-dimensional spherical shell. *Geophys. Res. Lett.*, 31(12), 2004.

[7] Masaki Yoshida and Akira Kageyama. Low-degree mantle convection with strongly temperature-and depth-dependent viscosity in a three-dimensional spherical shell. *J. Geophys. Res.*, 111, 2006.

[8] Takehiro Miyagoshi, Akira Kageyama, and Tetsuya Sato. Formation of current coils in geodynamo simulation. *submitted*, 2008.

[9] Masanori Kameyama, Akira Kageyama, and Tetsuya Sato. Multigrid iterative algorithm using pseudo-compressibility for three-dimensional mantle convection with strongly variable viscosity. *J. Comput. Phys.*, 206(1):162–181, 2005.

[10] Masanori Kameyama. ACuTEMan: A multigrid-based mantle convection simulation code and its optimization to the earth simulator. *J. Earth Simulator*, 4:2–10, 2005.

[11] M Kameyama and D A Yuen. 3-D convection studies on the thermal state in the lower mantle with post-perovskite phase transition. *Geophys. Res. Lett.*, 33, 2006.

[12] David A Yuen, Marc Monnereau, Ulrich Hansen, Masanori Kameyama, and Ctirad Matyska. Dynamics of superplumes in the lower mantle. *In D. A. Yuen, S. Maruyama, S. Karato, and B. F. Windley, editors, Superplumes: Beyond Plate Tectonics. Springer*, pages 239–268, 2007.

[13] David A Yuen, Ctirad Matyska, Ondrej Cadek, and Masanori Kameyama. The dynamical influences from physical properties in the lower mantle and post-perovskite phase transition. *In K. Hirose and D. A. Yuen, editors, The last phase transition, Geophysical Monograph. American Geophysical Union*, 2007.

[14] Masanori Kameyama. Simulation studies of solid earth dynamics on the earth simulator – theoretical backgrounds, tools and outcrops. *International COE of Flow Dynamics Lecture Series, Earth Simulator, Tohoku Univ. Press, Sendai, Japan*, 2008.

[15] Mikito Furuichi, Masanori Kameyama, and Akira Kageyama. Three-dimensional eulerian method for large deformation of viscoelastic fluid: Toward plate-mantle simulation. *J. Comput. Phys.*, 227:4977–4997, 2008.

[16] Kachishige Sato, Naoya Minagawa, Mamoru Hyodo, Toshitaka Baba, Takane Hori, and Yoshiyuki Kaneda. Effect of elastic inhomogeneity on the surface displacements in the northeastern japan: Based on three-dimensional numerical modeling. *Earth Planets Space*, 59(10):183–1093, 2007.

[17] Mamoru Hyodo and Kazuro Hirahara. Geofem kinematic earthquake cycle simulation in southwest japan. *Pure Appl. Geophys.*, 161:2069–2090, 2004.

[18] Yosuke Ito and Mitsuhiro Toriumi. Pressure effect of self-diffusion in periclase (MgO) by molecular dynamics. *J. Geophys. Res.*, 112(B4):7, 2007.

[19] Yosuke Ito. A computational study of the lower mantle rheology. *Ph.D thesis, Univ. Tokyo*, 2008.

[20] Nobuaki Ohno and Akira Kageyama. Introduction to virtual reality visualization by the CAVE system. *Advanced Methods for Space Simulations, edited by H.*

Usui and Y. Omura, *TERRAPUB*, *Tokyo*, pages 167–207, 2007.

[21] M. Damon, M. Kameyama, M. Knox, D. H. Porter, D. A. Yuen, and E. O. D. Sevre. Interactive visualization of 3D mantle convection. *Visual Geosciences*, pages doi:10.1007/s10069–007–0008–1, 2008.

先端的固体地球科学シミュレーションコードの開発

プロジェクト責任者
陰山　聡　海洋研究開発機構　地球シミュレータセンター

著者
陰山　聡*1，兵藤　守*1，古市　幹人*1，宮腰　剛広*1，大野　暢亮*1，亀山　真典*2，伊藤　洋介*3
*1　海洋研究開発機構　地球シミュレータセンター
*2　愛媛大学
*3　東京大学

我々の最終的な目標は、地球シミュレータ(ES)を駆使した大規模計算機シミュレーションを通じて、地球ダイナモとマントル対流をはじめとする地球内部全体の構造とダイナミクスを理解することである。そのために必要となる大規模並列計算手法や基本数値アルゴリズムの独自開発にも積極的に取り組んでいる。

地球ダイナモシミュレーション：前年度までに開発したインヤン格子を用いたダイナモコードにより、512ノード(4096プロセッサ)を中心とした本格的プロダクトランを実施した。インヤン格子ダイナモコードの特徴である高い並列計算性能により、高解像度計算が実現でき、その結果世界で最も低いエクマン数領域の地球ダイナモシミュレーションに成功した。その結果、このエクマン数領域ではジェット流を伴うシート・プルーム対流構造が形成されること、およびそれに伴いヘリカルコイル電流構造と磁束管構造が形成されることが分かった。これらはどれもこれまでの高いエクマン数領域のダイナモシミュレーションでは見られなかった現象である。

インヤン格子とACuTE法による3次元球殻マントル対流の高速シミュレーションプログラムの開発：昨年度より我々は、3次元球殻領域でのマントル対流の大規模並列シミュレーションを可能にすべく、新たなシミュレーションコードの開発を実施している。新たなコードは、インヤン格子とACuTE法という、我々が独自に開発した2つの計算手法を融合したもので、昨年度までにそのプロトタイプの構築が完了した。今年度は本コードの演算効率を左右する、流れ場解法ルーチンのベクトル化作業を集中的に実施した。この結果、有限体積法ベースのプログラムでは世界最高レベルの空間分解能をもつ3次元球殻マントル対流シミュレーションを実現することができた。またこれにより、本コードの系統的なベンチマークテストを高い空間分解能に至るまで実施し、その高い計算精度を改めて実証した。これと並行して、粘性率の空間変化に対する流れ場ソルバの頑健さの向上を図った結果、粘性率コントラスト1万倍程度で予想されている流れ場の長波長化を再現することができた。

マントル・プレート結合シミュレーションに向けたコード開発:大規模計算機シミュレーションにおいて、プレートテクトニクスを再現することを目的として、我々は大きく物性の異なるマントルとプレートを同時に扱うシミュレーション手法を開発している。本年度はこれまで開発してきた大きな粘性差を伴う粘弾性物質の大変形シミュレーション手法を用いて、大きな粘性差により再現されるfluid rope coiling現象を、まるで自由表面を扱っているかのように再現し、それらの解に定量的な評価を与えることに成功した。fluid rope coilingのような複雑な現象では比較すべき単純な解析解がないため定量的な比較は困難であったが、近年開発されたfluid ropeの1次元数値モデルを拡張して解くことで定量的な比較を可能にした。この研究により、我々のシミュレーションにより再現されるシャープな境界をもつプレートなどの振る舞いは、解析対象として定性的にも定量的にも信頼がおけるものであることを示せた。

地震サイクルシミュレーション関係の進捗：プレート沈み込みに伴う巨大地震の断層面への応力蓄積、そこでの地震発生による応力解放といったプレート境界で発生する一連のプロセスを計算機上で再現する試みは、地震サイクルシミュレーションと呼ばれる。先行研究では、媒質として、「ずれ」に対する応力応答の解析関数が分かっている均質半無限弾性媒質のような理想化媒質を仮定し、断層にわたる「ずれ」と「ずれ応答」との積の境界積分によって応力場を精度よく評価している。しかし、日本列島のような沈み込み帯では、地震波トモグラフィーから示唆される強い不均質構造が存在する。こういった解析的には「ずれ応答」が求まらない複雑な不均質構造を考慮し、その影響をシミュレーションに反映させることが、現実的なシミュレーションを実行するために不可欠である。つまり、1) 断層近傍の応力場を精度良く評価すること、2) 不均質弾性・粘弾性媒質の取り扱いが可能であること、の両者を満足する計算手法が必要となるが、境界積分方程式法・有限要素法などの単一の数値計算手法では、これらの両立は困難である。このため、両手法の長所のみを抽出・カップルさせる手法を、我々が開発している有限要素法ベースの地震サイクルシミュレーションコードに実装し、その有効性を検証した。手法の実装により、有限要素計算での断層近傍の空間離散化レベルにほぼ依存せず、一定の不均質媒質起源の断層応力変化が抽出可能となり、手法の有効性が検証できたと言える。

キーワード：地球ダイナモ, マントル対流, ACuTE法, インヤン格子, 粘弾性流体, 地震サイクルシミュレーション